© 2025. This manuscript version is made available under the CC-BY-NC-ND 4.0 license https://creativecommons.org/licenses/by-nc-nd/4.0/

Enhanced rate performance and specific capacity in Ti-

substituted P2-type layered oxide enabled by crystal structure

and particle morphology modifications

Hari Narayanan Vasavan^a, Manish Badole^a, Sushmita Dwivedi^a, Deepu Kumar^b, Pradeep

Kumar^b, and Sunil Kumar^{a,*}

^a Department of Metallurgy Engineering and Materials Science, Indian Institute of Technology

Indore, Simrol, 453552, India.

^b School of Basic Sciences, Indian Institute of Technology Mandi, Mandi, 175005, India

*Corresponding author.

E-mail address: sunil@iiti.ac.in

Abstract

In recent years, P2-type layered oxides have received considerable attention as potential

cathodes for Na-ion batteries owing to their compositional diversity, good specific capacity,

and cyclability. However, poor rate performance and low-capacity retention at high discharge

rates have limited their use in commercial battery applications. This study aims to mitigate this

issue by synthesizing a series of structurally engineered P2-type cathode materials, through Ti

with high cyclability substitution, and improved rate performance.

Na_{0.70}Ni_{0.20}Cu_{0.15}Mn_(0.65-x)Ti_xO₂ were prepared through a sol-gel route and were characterized

for their structural, electrical, and electrochemical properties In the Ti-substituted samples, the

Rietveld refinement of XRD data revealed an increased size of the bottleneck area of the Na-

O₆ prism planes, while the SEM images showed a decrease in the aspect ratio of hexagon-type

morphology of particles which facilitates faster Na-ion conduction through the material. These

1

changes in the crystal structure and particle morphology induced by Ti substitution have significantly improved electrical and electrochemical performance compared to the parent material. The sample with x = 7.5% exhibited a specific capacity of 126 mAh/g at a discharge rate of 0.1C in the 2.00 - 4.25 V window, which was about 25% more than that of the undoped material. At a discharge rate of 1C, the specific capacity of Na_{0.70}Ni_{0.20}Cu_{0.15}Mn_{0.575}Ti_{0.075}O₂ was 97 mAh/g compared to 74 mAh/g for Na_{0.70}Ni_{0.20}Cu_{0.15}Mn_{0.65}O₂ sample. Na_{0.70}Ni_{0.20}Cu_{0.15}Mn_(0.65-x)Ti_xO₂ samples also exhibited excellent cyclability, with over 95% of original capacity retained after 300 cycles. Complex impedance measurements corroborated the improved Na-ion conductivity in Ti-doped samples and an associated increase in Na-ion transference number from 0.86 for the sample with x = 0 to 0.97 for the sample with x = 0.075.

Keywords: Sol-gel process; Na-ion batteries; Layered oxides; Electrochemical behavior; Rate performance

1. Introduction

In recent years, rapid developments in Li-ion batteries (LIBs) have made them a popular choice for secondary energy storage applications [1-4]. However, as the demand for energy storage systems for mobility and portable electronics applications rises, scarcity of Li deposits and the issues related to Li recycling is expected to cause the demand for Li to exceed its supply, leading to high LIBs prices [3, 5, 6]. Na-ion batteries (NIBs) are widely regarded as a possible alternative to replace LIBs to meet future demands, especially in areas of stationary storage applications such as grid storage [5, 7, 8]. This is primarily because of the comparatively natural abundance of Na and the commonalities that NIBs share with LIBs in terms of components and manufacturing techniques, paving the way for their seamless integration into the current battery eco-systems [6, 9, 10].

Cathode materials being the primary source of ions play a pivotal role in deciding the performance and properties of ion storage batteries [11, 12]. In NIBs, the research is mainly focused on three types of cathodes: layered oxides (LOs), NASICON, and Prussian blue analogs (PBA). NASICON-type cathodes show good cyclability but have lower capacity. PBA cathodes, being cyanide-based, are toxic and difficult to handle [12, 13]. Layered oxides $(Na_xTMO_2; 0 \le x \le 1; TM$ - transition metal cation or a mixture of multiple cations) are one of the most extensively researched cathode materials for application in NIBs. These are known for their compositional diversity, high capacity, cyclability, and easier synthesis [12, 14]. Cathodes based on LOs have also been commercialized in LIBs; hence, certain aspects of the research in LIBS can be used for the development of the same in Na-ion batteries.

LOs are mainly classified into 4 types O2, P2, O3, and P3 (named based on the nomenclature developed by Delmas et al. [15]). Most of the LO cathodes synthesized are based on P2 and O3-type structures. O3 types usually have x > 0.8 and transform into a P3 type structure when x < 0.8. P2-type materials, on the other hand, have x < 0.8 and undergo an O2 transformation when x falls below 0.2 at high voltages [16, 17]. The transformation of LOs during cycling is detrimental to cyclic performance and can be avoided by controlling the cut-off voltage during charging in the case of P2-type materials as this structure is stable across a wider range of Na concentrations (0.8 < x < 0.2) [2, 17]. In the case of O3-type materials, the structural transformation is unavoidable owing to the transformation into a P3-type structure at low voltages [18]. In addition to better cyclic performance, P2-type materials also have larger interlayer spacing and lesser diffusion barriers to Na-ion conduction resulting in better rate capability [18, 19].

Among the combination of transition metals studied in P2-type materials, those based on Mn have received the most attention [14]. Manganese is an earth-abundant resource, and P2-type NaMn_xO₂ cathodes have been reported to show high capacities close to 200 mAh/g [11, 14].

However, Mn-based cathodes suffer from low OCVs (~3 V) due to the low oxidation potential of the Mn^{3+}/Mn^{4+} redox couple (typically between 2 – 3 V) and have poor cyclic performance due to detrimental distortions and phase transformations induced by Jahn-teller active Mn3+ ions at lower voltages [20-22]. Mn-based cathodes have been doped with other elements such as Ni and Cu to circumvent this problem. Ni and Cu ions exist predominantly in a 2+ oxidation state which forces Mn ions to maintain a 4+ oxidation state, which is Jahn teller inactive during charging/discharging. Ni²⁺-Ni⁴⁺ involves a 2-electron transfer as opposed to the one-electron transfer of the Mn³⁺/Mn⁴⁺ redox couple, which makes up for the reduction in specific capacity from the loss of active Mn³⁺/Mn⁴⁺ redox couples. Cu²⁺, on the other hand, is known to stabilize the P2 structure at higher voltages improving the cyclic performance and improving the stability of the material in the ambient environment [23-25]. Additionally, oxidation potentials of Ni^{2+} – Ni^{4+} (~ 3.2 V vs. Na/Na⁺) and Cu^{2+} / Cu^{3+} (~ 4 V vs. Na/Na⁺) are higher than that of the Mn³⁺/Mn⁴⁺ redox couple, which will improve the energy density exhibited by the cathode material [24, 25]. The synergy between each of the elements in the Na_x(Ni–Cu–Mn)O₂ system gives it better cyclic performance and specific capacity (90 mAh/g with an average potential of 3.4 V), as reported in the literature [24, 26, 27].

In this work, we have further substituted Mn⁴⁺ in Na_{0.70}Ni_{0.20}Cu_{0.15}Mn_{0.65}O₂ with Ti⁴⁺ ions to further refine the Na_x(Ni–Cu–Mn)O₂ system to achieve better capacity and rate performance. Ti⁴⁺ ions have been reported to stabilize the P2 structure at high voltages by forming pillars for TMO₆ slabs, reducing volume shrinkages during cycling. Their inclusion into the structural framework also allows the enlargement of the NaO₂ layers with the contraction of the TMO₆ octahedron allowing better conduction of Na ions, resulting in improved rate performance [28-30]. In addition, Ti⁴⁺ ions have been found to be effective in suppressing Na⁺ ion vacancy ordering in the material, which further improves Na ion conduction [28, 31]. This work reports on the effects of structural changes in Na_{0.70}Ni_{0.20}Cu_{0.15}Mn_(0.65-x)Ti_xO₂ (hereinafter, NNCMT-

x, x = 0, 0.025, 0.050, 0.075, and 0.100) on the electrochemical behaviour of these samples. To rationalize the improvement in electrochemical performance, the electrical properties have also been investigated by performing complex impedance spectroscopy and chronoamperometry on each of the samples. In addition, Ex-situ XRD analysis was also conducted on the samples at different stages of the charge/discharge cycle to identify the structural changes in the cathodes during cycling.

2. Experimental

2.1. Synthesis

The P2-type Na_{0.70}Ni_{0.20}Cu_{0.15}Mn_(0.65-x)Ti_xO₂ (x = 0, 0.025, 0.050, 0.075, and 0.100) materials were synthesised using a simple sol-gel method. Stoichiometric amounts of nickel acetate tetrahydrate, copper (II) nitrate trihydrate, manganese (II) acetate tetrahydrate, titanium (IV) bis(ammonium lactato)dihydroxide (50 wt% aq.), and sodium carbonate were dissolved in DI water and stirred for 6 h after which appropriate amounts of ethylene glycol and citric acid were added. The resulting solution was continuously stirred for 12 h, followed by heating at ~ 80 °C to obtain a gel. The gel was dried, ground, and heat-treated at 500 °C for 12 h. The resulting powder was ground again and calcinated at different temperatures (700 – 1000 °C) for 12 h in air to obtain the final product.

2.2. Characterization

The room temperature crystal structures of the samples were characterized using powder x-ray diffraction (XRD) by employing an Empyrean, Malvern Pan analytical diffractometer, with Cu-Kα radiation source in the 2θ range of 10°- 80° and The crystallographic parameters of all samples were estimated from the Rietveld refinement of the XRD data using the software package *TOPAS Academic* (version 6) [32]. A field emission scanning electron microscopy (model JEOL-7610) equipped with energy-dispersive x-ray spectroscopy (EDS) was used to

study the morphology and distribution of constituent elements of powder samples. XPS measurements were taken using Thermofisher Scientific (Naxsa base) with an Al Kα X-ray source (1486.6 eV). For impedance studies, calcined powders were pressed into cylindrical pellets and sintered at 900 °C for 12 h. The sintered pellets were polished flat, electroded with silver paste on either side, and were cured at 650 °C for 10 min after drying. Impedance measurements were done on the pellets using a computer-controlled LCR meter (model: ZM 2376, NF Corp.) by applying a 50mV ac signal in the 1 Hz – 1 MHz frequency range. Chronoamperometry measurements were performed on the silver electroded samples using the Keithley Source Meter Unit (model 2450-EC) with 1 V applied across the sample.

For electrochemical studies, CR-2032 coin cells were fabricated using Na metal as the counter electrode, Celgard 2400 as the separator, and 1M NaBF4 in tetraethylene glycol dimethyl ether (tetraglyme) as the electrolyte. The cathode was prepared by mixing 85 wt.% active material, 5 wt.% Ketjen black, and 10 wt.% CMC binder in DI water. The slurry was then coated on an Al current collector and dried at 100 °C for 8 h in a vacuum oven. The cyclic voltammetry (CV) tests were performed on the coin cell using a Keithley source meter unit (Model 2450-EC) between 2.00 V to 4.25 V with a scan rate of 0.1 mV/s. Galvanometric charge-discharge tests were carried out using a Landt battery testing system (LANHE CT, 2001A). The rate performance tests were performed at 0.1C, 0.2C, 0.3C, 0.5C, 1C, 2C, and 3C, while the cyclic performance was evaluated at 1C for 300 cycles between 2.00 V to 4.25 V. The mass loading for each of the samples was ~ 2 mg/cm², and all C-rates were taken based on a specific capacity of 125 mAh/g.

3. Results and Discussion

3.1. XRD

Figure 1 shows the phase evolution of NNCMT-x (x = 0, 0.050, and 0.100) with the increase in calcination temperature. The XRD patterns show a rise in the intensity of peaks relating to the P2-type phase with the increase in calcination temperatures. Sample with the composition corresponding to x = 0.100 shows a minor O3 phase which is estimated to be about 3 wt. % of the sample. At calcination temperatures above 900 °C, a small CuO impurity phase was found in the Ti substituted samples. Initial analysis of the XRD patterns showed that Ti substitution was effective in decreasing the calcination temperatures of the parent material. The optimal calcination temperature decreases from 850 °C for x = 0 & 0.025 samples to 800 °C for samples with x = 0.05, 0.075, and 0.100.

The Rietveld refinement of the XRD data was utilized to determine the crystal structure of asprepared NNCMT samples. The experimental data along with the refinement profiles for two representative samples (x = 0 and x = 0.075) are shown in Fig. 2 and for x = 0.025, 0.050, and 0.100 samples are provided in the Supplementary Information (Fig. S1). The refinement of the XRD data confirms that all samples crystallize in the P2-type phase with hexagonal symmetry (P6s/mmc space group). A few minor peaks associated with the O3-type phase are also observed in the XRD pattern of the x = 0.100 sample. The weight fraction of the O3 phase in this sample was estimated to be ~ 5 % of the sample. The two minor peaks at $\sim 27.2^{\circ}$ and 28.3° in the XRD pattern of the x = 0 sample (marked by the * symbol in Fig. 2) correspond to superlattice reflections caused by the in-place Na-ion vacancy ordering [28, 33, 34]. Vacancy ordering of Na-ions in layered oxides is known to hider Na-ion diffusion and induce phase transformations during cycling [35, 36]. The intensities of these peaks decreased gradually with the increase in Ti concentration, suggesting the successful suppression of Na-ion vacancy ordering by Ti ions in the material, which concurs with the findings reported in the literature [37, 38].

Various crystallographic parameters obtained from the Rietveld refinement of the XRD data for all samples are provided in Tables 1 and Tables S (1-6). An increase in the lattice parameter a, a decrease in the lattice parameter c, and an overall increase in volume V of the hexagonal unit cell are seen with the increase in the concentration of Ti in NNCMT-x. This is due to the larger size of Ti⁴⁺ (0.605 Å in 6 coordination) compared to the Mn⁴⁺ (0.530 Å in 6 coordination)[37, 39, 40]. Further analysis of the XRD refinement data using VESTA revealed an increase in the area of the lateral faces of Na-O₆ prisms (Fig. 3) with the increase in Ti concentration [41]. Accordingly, the rectangular bottleneck for the sodium intercalation at the Na1 site increased from 11.03 Å² for NNCMT-0 to 11.47 Å² for the NNCMT-0.100 sample. In addition, the volume of TM-O₆ octahedron for NNCMT-0 is calculated to be $\sim 8.53 \text{ Å}^3$ which decreases to $\sim 8.36 \text{ Å}^3$ for the 10% Ti-doped sample, whereas, the volume of the Na-O₆ prisms increased from 13.83 Å³ to 14.09 Å³. Similar expansions of Na-O₂ layers accompanied with contractions of TM-O₂ layers upon Ti-substitution for Mn in layered oxides have been observed in earlier work [28]. The increase in the area of the lateral faces of Na-O₆ prisms is significant as it is expected to facilitate the conduction of Na-ions through the material by increasing the size of the rectangular bottleneck formed by the oxygen ions. This is substantiated by the improvement in electrical and electrochemical properties of the Ti-doped samples (discussed later in the text).

Table 1. Lattice parameters of NNCMT-*x* samples obtained from Rietveld refinement of room temperature XRD data.

a (Å)	c (Å)	$V(\mathring{\mathbf{A}}^3)$	Factors
2.8934	11.1660	80.9559	Rexp: 2.02
0.0001	± 0.0004	$\pm~0.0007$	Rwp: 3.82
,	a (Å) 2.8934 -0.0001	2.8934 11.1660	2.8934 11.1660 80.9559

					Rp : 2.65
					GOF: 1.89
					Rexp : 2.49
	0.025	2.9006	11.1357	81.1400	Rwp: 4.27
<i>x</i> =	0.025	$\pm\ 0.0004$	± 0.0002	$\pm\ 0.0003$	Rp: 2.86
					GOF: 1.72
					Rexp : 2.47
x = 0.050		2.9044	11.1318	81.3260	Rwp: 4.50
		$\pm~0.0006$	± 0.0003	$\pm\ 0.0004$	Rp: 2.88
					GOF: 1.82
					Rexp : 2.57
x = 0.075		2.9063	11.1276	81.4002	Rwp: 4.69
		$\pm\ 0.0004$	± 0.0002	$\pm\ 0.0003$	Rp: 2.99
					GOF: 1.82
P2 (96.4 % x = 0.100	D2 (0(4.9/)	2.9041	11.1485	81.4290	Rexp : 2.60
	P2 (96.4 %)	$\pm\ 0.0007$	$\pm \ 0.0004$	$\pm~0.0005$	Rwp: 4.19
		2.0525	16 2764	122 (242	Rp: 2.90
	O3 (3.6%)	2.9525	16.3764	123.6342	GOF: 1.62
J	, ,	$\pm\ 0.0006$	± 0.0004	$\pm\ 0.0006$	

3.2. Microstructure

The SEM micrographs of x = 0, 0.050, and 0.075 samples along with the representative elemental maps for the x = 0.075 sample are shown in Fig. 4. The SEM images for the x = 0.025 and 0.100 are given in Fig. S2. The elemental mapping indicates a uniform distribution of all the elements throughout the sample without any noticeable segregation. The SEM micrographs show a distinct change in morphology of powder particles with the increase in Ti substitution. The parent material was observed to have thinner hexagonal plates with sharper facets and large aspect ratios (close to 8), while the Ti substituted samples show thicker

particles with rounded edges and lower aspect ratios (close to 1). The average particle size (in the bigger (001) surface) was estimated to decrease from $\sim 1.9 \mu m$ for the undoped (x = 0) sample to $\sim 0.9 \mu m$ for the x = 0.075 sample, while the average thickness increased from ~ 0.25 μm in the former to $\sim 0.85 \mu m$ in the latter.

The hexagonal plate-type morphology of the NNCMT sample can be explained by the relatively lower surface energy of (001) and (00 $\bar{1}$) surfaces as compared to (100), (010), (110), ($\bar{1}00$), (0 $\bar{1}0$), and ($\bar{1}\bar{1}0$) surfaces. Accordingly, the equilibrium shape of NNCMT crystals will be dominated by (001) and (00 $\bar{1}$) surfaces resulting in a hexagonal plate-like morphology with a large aspect ratio (Fig. 4(a)). The change in the morphology of the Ti substituted samples suggests that the introduction of Ti⁴⁺ ions could increase the relative surface energies of (001) and (00 $\bar{1}$) surfaces, and consequently, a decrease in the aspect ratios. It should be noted that in P2-type material, the diffusion of Na-ion is predominantly in the basal planes. The increase in relative area of (100), (010), (110), ($\bar{1}00$), (0 $\bar{1}0$), and ($\bar{1}\bar{1}0$) surfaces is expected to facilitate faster Na-ion intercalation, which should result in better rate performances of the cathode material.

3.3. XPS

X-ray photoelectron spectroscopy (XPS) was performed to verify the oxidation states of constituent transition metals in NNCMT samples. Figure 5 compares the XPS spectra of Ni 2p, Mn 2p, Cu 2p, and Ti 2p in different samples. The four characteristic peaks in the Ni2p spectra are attributed to Ni 2p_{3/2} (~ 855 eV), Ni 2p_{1/2}(~ 872 eV), and their shake-up satellite peaks which indicates that Ni maintained a +2 oxidation state in all samples [27, 42, 43]. The two peaks in the Cu 2p spectra centered at ~ 933 and ~ 953 eV correspond to Cu 2p_{3/2} and Cu 2p_{1/2}, respectively, suggesting that Cu also has a +2 oxidation in all the materials [27, 42, 43]. The Mn 2p spectra can be deconvoluted into 2 peaks at ~ 643 eV (Mn 2p_{3/2}) and ~ 654 eV (Mn

2p_{1/2}) confirming the existence Mn⁴⁺ ions in the samples [27, 42, 43]. The Ti 2p_{3/2} and Ti 2p_{1/2} peaks located at 458 and 464 eV in the Ti 2p spectra indicate the presence of Ti⁴⁺ ions in the Ti-doped samples [42, 43]. The XPS spectra of all other elements in the Ti-doped samples were found to be identical to that of the parent composition, indicating that Ti doping did not affect the oxidation states of any of the elements present in these samples.

3.4. CV

To investigate the redox process in the prepared cathode materials, cyclic voltammetry (CV) was performed on the half-cells between a potential window of 2.00 - 4.25 V with a scan rate of 0.1 mV/s. The CV profiles of the first 3 cycles for the x = 0 and 0.075 samples are shown in Fig. 6, and that of x = 0.025, 0.050, and 0.100 are given in Fig. S3. The minor peaks observed below 3 V for all cathodes can be related to Mn³⁺/Mn⁴⁺ redox processes [24, 44]. As mentioned before, Ti⁴⁺ ions do not show any redox activity in the 2.00 - 4.25 V potential range and, hence, remain largely electrochemically inactive [38, 45]. For x = 0 sample, two peaks centred at \sim 3.45 V and \sim 3.68 V are attributed to Ni2+/Ni4+ redox reaction and Na-ion vacancy ordering [37, 38]. In contrast, Ni^{2+}/Ni^{4+} redox peaks in the Ti substituted samples are located at ~ 3.2 V, and the peaks related to Na-ion vacancy ordering almost vanish which concurs with the observed decrease in the intensity of the vacancy ordering related superlattice reflections in the XRD patterns. The activation of the $Cu^{2+/3+}$ redox couple is evidenced by the peak at ~3.9 V in the CV curves [24, 25, 46]. Cu redox activity around 3.9 V in P2-type LOs is also reported by Chen et al. using XPS data [47, 48]. The pseudo plateaus of Cu^{2+/3+} and that of Ni^{4+/2+} have been marked in the discharge curves shown in Fig. 7(a). The CV profiles for the second and third cycles of all the cathodes almost coincided indicating excellent reversibility of all the redox processes.

3.5. GCD

The galvanostatic charge/discharge (GCD) profiles of all samples between 2.00 – 4.25 V at discharge rates of 0.1C and 1C are displayed in Fig. 7 (a) & (b). The discharge profiles show a slow voltage drop with an increase in capacity between 4 V to 3 V, where Ni^{4+/2+} and Cu^{3+/2+} redox activity was observed in the CV profiles. The voltage drop becomes more drastic between 3 V to 2 V due to the smaller number of Mn^{4+/3+} redox couples. It is interesting to note that all the Ti substituted samples exhibited higher specific capacities compared to the unsubstituted sample at different discharge rates. At 0.1C rate, x = 0.1 and 0.075 samples showed a specific capacity of ~ 127 mAh/g which is about 28% more than the unsubstituted sample (i.e., composition with x = 0). As the discharge rate was increased from 0.1C to 1C, the x = 0.075 sample showed the lowest drop in specific capacity among all samples. The specific capacity is close to 97 mAh/g, which is about 31% more than that of the unsubstituted sample at the same discharge rate of 1C. These results are significant as Ti ions being lighter than their Mn counterparts, were estimated to increase the specific capacity by a margin of only 2-3 %, but an increase in 27% of specific capacity at 0.1C and a subsequent jump of 31% at 1C rate is not expected from the simple gravimetric consideration. Such improvements in specific could be attributed to the change in morphology of the particles and increase in the area of bottlenecks along conduction pathways reported in Ti-doped samples. These modifications facilitate faster movement of Na-ions during sodiation and desodiation, allowing for faster and greater extraction of Na ions leading to higher capacity and rate performance. Fig. 7(c) shows the rate capability of all five cathodes cycled between 2.00 – 4.25 V at different C-rates in 0.1C - 3C range. While cycling back to lower discharge rates, all samples exhibited their initial specific capacities without any significant loss in capacity, indicating high reversibility at varying discharge rates. The difference between the discharge specific capacities of x = 0.075 and x =0 samples was observed to increase with an increase in C-rates. The charge retention capacity of all five samples after 300 cycles at 1C is shown in Fig. 7(d). All samples exhibit excellent cyclability with over 95% specific capacity retained after 300 cycles.

To study the structural evolution of the cathode materials during Na-ion insertion and extraction, ex-situ XRD was performed on x = 0.075 sample, and the result is shown in Fig. 8. The XRD plots of both the samples show a gradual shift in the (002) and (004) peaks to lower angles during charging. This is due to an increase in lattice parameters caused by higher repulsion between TM ions during the extraction of Na⁺ ions from the material which is reported in other P2-type materials [44, 49, 50]. After discharging, these peaks were observed to shift towards their initial positions indicating high reversibility of the intercalation and deintercalation processes and good structural stability of the layered oxide. The broadening of the (00*l*) peaks observed in the XRD patterns with an increase in voltage from 2 V to 3.7 V is due to the lattice strain generated in the crystal structure with the removal of Na-ions. As the Na-ions are removed from the lattice, the unit cells that have lost Na-ions expand along the caxis (which is evident from the shifting of (00l) peaks towards lower angles) while the unit cells that have retained their Na ions do not. This mismatch in interplanar spacing across unit cells generates the lattice strain and is reflected in the broadening of the XRD peaks. As the voltage is further increased to 4.2 V, the majority of unit cells in NNCMT become devoid of Na-ions, leading to a more uniform expansion of unit cells across the sample, which consequently causes a reduction in non-uniform lattice strain. This is evidenced by lower FWHM for the (004) peak in the XRD pattern for the sample charged to 4.2 V than that of the sample charged to 3.7 V (Fig. 8(a2)). The observed asymmetry in the NNCMT peaks and a clear splitting of the peak at 65° (from the Aluminum current collector) is due to the contribution of the Cu-Kal and Cu-Ka2 emission profile of the X-ray diffractometer. Apart from the peak shifts and their broadening, no new peaks corresponding to phase transformation were observed, confirming the existence of a single P2 phase throughout the charging and

discharging process, which could be the reason behind the high cyclic performance of the cathode [44, 50].

3.6. EIS

To rationalize the improvement in electrochemical performance, the change in electrical properties of the samples was probed by performing complex impedance spectroscopy on the pelletized samples sintered at 900 °C for 12 h. The room temperature Nyquist plots obtained for different samples along with the equivalent circuit used to fit the impedance data are shown in Fig. S4. The plots show a decreasing trend in the overall resistance value of the samples with the increase in Ti substitution. Nyquist plots for all samples show a linear tail component in the lower frequency region which is a typical feature of ion-blocking at the sample-electrode interface. Such a feature indicates substantial Na-ion conduction in these samples [51-53]. The values of the total conductivity calculated from the fitted equivalent circuit data for all compositions under investigation are given in Table 2. To quantify the extent of Na-ion conduction at room temperature in these samples, chronoamperometry was performed under 1 V (Fig. S5). The Na-ion transference numbers (t_{Na+}) for different samples obtained from their respective chronoamperometry curves are also provided in Table 2. The increasing trend in the conductivity and t_{Na+} values of the Ti substituted samples can be attributed to the increase in the area of lateral faces of the Na-O₆ prisms of the unit cell and the favorable change in the crystal morphology in Ti-substituted samples.

Table 2. Room temperature (RT) conductivity and Na-ion transference number (t_{Na^+}) of Na_{0.67}Ni_{0.20}Cu_{0.15}Mn_(0.65-x)Ti_xO₂ samples

Sample	RT Conductivity	Transference Number (t _{Na+})	
x = 0	4.03 × 10 ⁻⁶ S/cm	0.86	

x = 0.025	$7.35 \times 10^{-6} \text{ S/cm}$	0.91
x = 0.050	$1.11 \times 10^{-5} \text{ S/cm}$	0.95
x = 0.075	$3.07 \times 10^{-5} \text{ S/cm}$	0.97
x = 0.100	$4.53 \times 10^{-5} \text{ S/cm}$	0.96

The materials were also tested for their moisture stability, for which the powder samples were stored under DI water for 3 h and then dried in a vacuum oven at 100 °C for 5 h. The XRD patterns of the water-treated samples with x = 0, 0.05, and 0.100 are shown in Fig. S6. The patterns show no impurity peaks and match with the patterns of their respective as-prepared samples indicating the materials are water stable.

4. Conclusions

To summarize, Ti substituted P2 type-Na_{0.70}Ni_{0.20}Cu_{0.15}Mn_{0.65-x}Ti_xO₂ materials were prepared via a sol-gel route. Analysis of XRD patterns and FESEM images showed improvements in the size of conduction bottlenecks and morphology along with the successful suppression of Naion vacancy ordering in Ti substituted samples. The improvement in Na-ion diffusion in Tidoped samples caused by Ti-induced modifications to the morphology and crystal structure was evidenced by the increase in ionic conductivity and Na-ion transference number. On cycling between 2 – 4.25 V, x = 0.075 sample showed the highest specific capacity of 127 mAh/g at 0.1C, which is about 27% higher than that for the undoped sample. Even at a higher discharge rate of 1C, Na_{0.70}Ni_{0.20}Cu_{0.15}Mn_{0.575}Ti_{0.075}O₂ showed a capacity of 97 mAh/g as compared to 74 mAh/g that of the x = 0 sample. Further, this sample retained more than 95% of its initial capacity after 300 cycles at 1C. Apart from exhibiting an improved specific capacity, excellent cyclability, and good rate performance, Na_{0.70}Ni_{0.20}Cu_{0.15}Mn_{0.575}Ti_{0.075}O₂

was found to be stable in moisture, making it an attractive candidate as a Na-ion battery cathode.

Acknowledgments

The authors thank Science and Engineering Research Board (SERB), India, for the financial support (grant number: CRG/2021/005548).

References

[1] K. Divya, J. Østergaard, Battery energy storage technology for power systems—An overview, Electric power systems research 79(4) (2009) 511-520.

https://doi.org/https://doi.org/10.1016/j.epsr.2008.09.017.

[2] N. Yabuuchi, K. Kubota, M. Dahbi, S. Komaba, Research Development on Sodium-Ion Batteries, Chemical Reviews 114(23) (2014) 11636-11682.

https://doi.org/https://doi.org/10.1021/cr500192f.

[3] D. Larcher, J.M. Tarascon, Towards greener and more sustainable batteries for electrical energy storage, Nature Chemistry 7(1) (2015) 19-29.

https://doi.org/https://doi.org/10.1038/nchem.2085.

[4] P. Denholm, E. Ela, B. Kirby, M. Milligan, The Role of Energy Storage with Renewable Electricity Generation, (2010). https://doi.org/https://doi.org/10.2172/972169.

[5] J.-Y. Hwang, S.-T. Myung, Y.-K. Sun, Sodium-ion batteries: present and future, Chemical Society Reviews 46(12) (2017) 3529-3614.

https://doi.org/https://doi.org/10.1039/C6CS00776G.

[6] Mineral commodity summaries 2021, Mineral Commodity Summaries, Reston, VA, 2021, p. 200.

[7] V. Palomares, P. Serras, I. Villaluenga, K.B. Hueso, J. Carretero-González, T. Rojo, Naion batteries, recent advances and present challenges to become low cost energy storage systems, Energy & Environmental Science 5(3) (2012) 5884-5901.

https://doi.org/https://doi.org/10.1039/C2EE02781J.

[8] X. Xiang, K. Zhang, J. Chen, Recent Advances and Prospects of Cathode Materials for Sodium-Ion Batteries, Advanced Materials 27(36) (2015) 5343-5364.

https://doi.org/https://doi.org/10.1002/adma.201501527.

[9] C. Vaalma, D. Buchholz, M. Weil, S. Passerini, A cost and resource analysis of sodiumion batteries, Nature Reviews Materials 3(4) (2018) 18013.

https://doi.org/https://doi.org/10.1038/natrevmats.2018.13.

- [10] J. Peters, A. Cruz, M. Weil, Exploring the Economic Potential of Sodium-Ion Batteries, Batteries 5 (2019) 10. https://doi.org/https://doi.org/10.3390/batteries5010010.
- [11] R.J. Clément, P.G. Bruce, C.P. Grey, Review—Manganese-Based P2-Type Transition Metal Oxides as Sodium-Ion Battery Cathode Materials, Journal of The Electrochemical Society 162(14) (2015) A2589-A2604. https://doi.org/https://doi.org/10.1149/2.0201514jes.
- [12] E. Goikolea, V. Palomares, S. Wang, I.R. de Larramendi, X. Guo, G. Wang, T. Rojo, Na-Ion Batteries—Approaching Old and New Challenges, Advanced Energy Materials 10(44) (2020) 2002055. https://doi.org/https://doi.org/10.1002/aenm.202002055.
- [13] R. Usiskin, Y. Lu, J. Popovic, M. Law, P. Balaya, Y.-S. Hu, J. Maier, Fundamentals, status and promise of sodium-based batteries, Nature Reviews Materials 6(11) (2021) 1020-1035. https://doi.org/https://doi.org/10.1038/s41578-021-00324-w.
- [14] J. Darga, J. Lamb, A. Manthiram, Industrialization of Layered Oxide Cathodes for Lithium-Ion and Sodium-Ion Batteries: A Comparative Perspective, Energy Technology 8(12) (2020) 2000723. https://doi.org/https://doi.org/10.1002/ente.202000723.
- [15] C. Delmas, C. Fouassier, P. Hagenmuller, Structural classification and properties of the layered oxides, Physica B+C 99(1) (1980) 81-85.

https://doi.org/https://doi.org/10.1016/0378-4363(80)90214-4.

[16] C. Zhao, Z. Yao, Q. Wang, H. Li, J. Wang, M. Liu, S. Ganapathy, Y. Lu, J. Cabana, B. Li, X. Bai, A. Aspuru-Guzik, M. Wagemaker, L. Chen, Y.-S. Hu, Revealing High Na-Content P2-Type Layered Oxides as Advanced Sodium-Ion Cathodes, Journal of the American Chemical Society 142(12) (2020) 5742-5750.

https://doi.org/https://doi.org/10.1021/jacs.9b13572.

[17] P.-F. Wang, Y. You, Y.-X. Yin, Y.-S. Wang, L.-J. Wan, L. Gu, Y.-G. Guo, Suppressing the P2–O2 Phase Transition of Na_{0.67}Mn_{0.67}Ni_{0.33}O₂ by Magnesium Substitution for Improved Sodium-Ion Batteries, Angewandte Chemie International Edition 55(26) (2016) 7445-7449. https://doi.org/https://doi.org/10.1002/anie.201602202.

[18] J. Liu, W.H. Kan, C.D. Ling, Insights into the high voltage layered oxide cathode materials in sodium-ion batteries: Structural evolution and anion redox, Journal of Power Sources 481 (2021) 229139. https://doi.org/https://doi.org/10.1016/j.jpowsour.2020.229139. [19] S. Guo, Y. Sun, J. Yi, K. Zhu, P. Liu, Y. Zhu, G.-z. Zhu, M. Chen, M. Ishida, H. Zhou, Understanding sodium-ion diffusion in layered P2 and P3 oxides via experiments and first-principles calculations: a bridge between crystal structure and electrochemical performance, NPG Asia Materials 8(4) (2016) e266-e266.

https://doi.org/https://doi.org/10.1038/am.2016.53.

[20] D. Kundu, E. Talaie, V. Duffort, L.F. Nazar, The Emerging Chemistry of Sodium Ion Batteries for Electrochemical Energy Storage, Angewandte Chemie International Edition 54(11) (2015) 3431-3448. https://doi.org/https://doi.org/10.1002/anie.201410376.

[21] J. Billaud, R.J. Clément, A.R. Armstrong, J. Canales-Vázquez, P. Rozier, C.P. Grey, P.G. Bruce, β-NaMnO₂: A High-Performance Cathode for Sodium-Ion Batteries, Journal of the American Chemical Society 136(49) (2014) 17243-17248.

https://doi.org/https://doi.org/10.1021/ja509704t.

[22] D. Su, C. Wang, H.-j. Ahn, G. Wang, Single Crystalline Na_{0.7}MnO₂ Nanoplates as Cathode Materials for Sodium-Ion Batteries with Enhanced Performance, Chemistry – A European Journal 19(33) (2013) 10884-10889.

https://doi.org/https://doi.org/10.1002/chem.201301563.

[23] Y. Zhang, R. Zhang, Y. Huang, Air-Stable Na_xTMO₂ Cathodes for Sodium Storage, Frontiers in Chemistry 7 (2019). https://doi.org/https://doi.org/10.3389/fchem.2019.00335.

[24] L. Wang, Y.-G. Sun, L.-L. Hu, J.-Y. Piao, J. Guo, A. Manthiram, J. Ma, A.-M. Cao, Copper-substituted Na_{0.67}Ni_{0.3-x}Cu_xMn_{0.7}O₂ cathode materials for sodium-ion batteries with suppressed P2–O2 phase transition, Journal of Materials Chemistry A 5(18) (2017) 8752-8761. https://doi.org/https://doi.org/10.1039/C7TA00880E.

[25] Y. Li, Z. Yang, S. Xu, L. Mu, L. Gu, Y.-S. Hu, H. Li, L. Chen, Air-Stable Copper-Based P2-Na_(7/9)Cu_(2/9)Fe_(1/9)Mn_(2/3)O₍₂₎ as a New Positive Electrode Material for Sodium-Ion Batteries, Advanced Science, 2(6) (2015) 1500031-1500031.

https://doi.org/https://doi.org/10.1002/advs.201500031.

[26] P. Ma, W. Kang, Y. Wang, D. Cao, L. Fan, D. Sun, Binary metal co-substituted P2-type Na_{0.67}Mn_{0.7}Cu_{0.15}Ni_{0.15}O₂ microspheres as robust cathode for high-power sodium ion battery, Applied Surface Science 529 (2020) 147105.

https://doi.org/https://doi.org/10.1016/j.apsusc.2020.147105.

[27] W. Kang, D.Y.W. Yu, P.-K. Lee, Z. Zhang, H. Bian, W. Li, T.-W. Ng, W. Zhang, C.-S. Lee, P2-Type Na_xCu_{0.15}Ni_{0.20}Mn_{0.65}O₂ Cathodes with High Voltage for High-Power and Long-Life Sodium-Ion Batteries, ACS Applied Materials & Interfaces 8(46) (2016) 31661-31668. https://doi.org/https://doi.org/10.1021/acsami.6b10841.

[28] P.-F. Wang, H.-R. Yao, X.-Y. Liu, Y.-X. Yin, J.-N. Zhang, Y. Wen, X. Yu, L. Gu, Y.-G. Guo, Na⁺ vacancy disordering promises high-rate Na-ion batteries, Science Advances 4(3) (2018) eaar6018. https://doi.org/https://doi.org/10.1126/sciadv.aar6018.

[29] H. Yoshida, N. Yabuuchi, K. Kubota, I. Ikeuchi, A. Garsuch, M. Schulz-Dobrick, S. Komaba, P2-type Na_{2/3}Ni_{1/3}Mn_{2/3-x}Ti_xO₂ as a new positive electrode for higher energy Na-ion batteries, Chemical Communications 50(28) (2014) 3677-3680.

https://doi.org/https://doi.org/10.1039/C3CC49856E.

[30] Z. Cao, L. Li, C. Zhou, X. Ma, H. Wang, Contribution of titanium substitution on improving the electrochemical properties of P2-Na_{0.67}Ni_{0.33}Mn_{0.67}O₂ cathode material for

sodium-ion storage, Functional Materials Letters 13(03) (2020) 2051010. https://doi.org/10.1142/s1793604720510108.

[31] S. Tao, W. Zhou, D. Wu, Z. Wang, B. Qian, W. Chu, A. Marcelli, L. Song, Insights into the Ti⁴⁺ doping in P2-type Na_{0.67}Ni_{0.33}Mn_{0.52}Ti_{0.15}O₂ for enhanced performance of sodium-ion batteries, Journal of Materials Science & Technology 74 (2021) 230-236.

https://doi.org/https://doi.org/10.1016/j.jmst.2020.06.055.

[32] A. Coelho, TOPAS and TOPAS-Academic: an optimization program integrating computer algebra and crystallographic objects written in C++, Journal of Applied Crystallography 51(1) (2018) 210-218.

https://doi.org/https://doi.org/10.1107/S1600576718000183.

[33] D.H. Lee, J. Xu, Y.S. Meng, An advanced cathode for Na-ion batteries with high rate and excellent structural stability, Physical Chemistry Chemical Physics 15(9) (2013) 3304-3312. https://doi.org/https://doi.org/10.1039/C2CP44467D.

[34] R. Berthelot, D. Carlier, C. Delmas, Electrochemical investigation of the P2–Na_xCoO₂ phase diagram, Nature Materials 10(1) (2011) 74-80.

https://doi.org/https://doi.org/10.1038/nmat2920.

[35] A. Gutierrez, W.M. Dose, O. Borkiewicz, F. Guo, M. Avdeev, S. Kim, T.T. Fister, Y. Ren, J. Bareño, C.S. Johnson, On Disrupting the Na⁺-Ion/Vacancy Ordering in P2-Type Sodium–Manganese–Nickel Oxide Cathodes for Na⁺-Ion Batteries, The Journal of Physical Chemistry C 122(41) (2018) 23251-23260.

https://doi.org/https://doi.org/10.1021/acs.jpcc.8b05537.

[36] A.J. Toumar, S.P. Ong, W.D. Richards, S. Dacek, G. Ceder, Vacancy Ordering in O3-Type Layered Metal Oxide Sodium-Ion Battery Cathodes, Physical Review Applied 4(6) (2015) 064002. https://doi.org/https://doi.org/10.1103/PhysRevApplied.4.064002.

[37] K. Tang, Y. Huang, X. Xie, S. Cao, L. Liu, H. Liu, Z. Luo, Y. Wang, B. Chang, H. Shu, X. Wang, Electrochemical performance and structural stability of air-stable Na_{0.67}Ni_{0.33}Mn_{0.67-x}Ti_xO₂ cathode materials for high-performance sodium-ion batteries, Chemical Engineering Journal 399 (2020) 125725.

https://doi.org/https://doi.org/10.1016/j.cej.2020.125725.

[38] Q. Pei, M. Lu, Z. Liu, D. Li, X. Rao, X. Liu, S. Zhong, Improving the Na_{0.67}Ni_{0.33}Mn_{0.67}O₂ Cathode Material for High-Voltage Cyclability via Ti/Cu Codoping for Sodium-Ion Batteries, ACS Applied Energy Materials 5(2) (2022) 1953-1962. https://doi.org/https://doi.org/10.1021/acsaem.1c03466.

[39] J.-k. Park, G.-g. Park, H.H. Kwak, S.-T. Hong, J.-w. Lee, Enhanced Rate Capability and Cycle Performance of Titanium-Substituted P2-Type Na_{0.67}Fe_{0.5}Mn_{0.5}O₂ as a Cathode for Sodium-Ion Batteries, ACS Omega 3(1) (2018) 361-368.

https://doi.org/https://doi.org/10.1021/acsomega.7b01481.

[40] R. Shannon, Revised effective ionic radii and systematic studies of interatomic distances in halides and chalcogenides, Acta Crystallographica Section A 32(5) (1976) 751-767. https://doi.org/doi:10.1107/S0567739476001551.

[41] K. Momma, F. Izumi, VESTA 3 for three-dimensional visualization of crystal, volumetric and morphology data, Journal of Applied Crystallography 44(6) (2011) 1272-1276. https://doi.org/https://doi.org/10.1107/S0021889811038970.

[42] J.F. Moulder, J. Chastain, Handbook of X-ray Photoelectron Spectroscopy: A Reference Book of Standard Spectra for Identification and Interpretation of XPS Data, Physical Electronics Division, Perkin-Elmer Corporation 1992.

[43] S. Hüfner, Photoelectron spectroscopy: principles and applications, Springer Science & Business Media 2013.

[44] L. Yang, S.-h. Luo, Y. Wang, Y. Zhan, Q. Wang, Y. Zhang, X. Liu, W. Mu, F. Teng, Cu-doped layered P2-type Na_{0.67}Ni_{0.33-x}Cu_xMn_{0.67}O₂ cathode electrode material with enhanced electrochemical performance for sodium-ion batteries, Chemical Engineering Journal 404 (2021) 126578. https://doi.org/https://doi.org/10.1016/j.cej.2020.126578. [45] M.H. Han, E. Gonzalo, N. Sharma, J.M. López del Amo, M. Armand, M. Avdeev, J.J. Saiz Garitaonandia, T. Rojo, High-Performance P2-Phase Na_{2/3}Mn_{0.8}Fe_{0.1}Ti_{0.1}O₂ Cathode Material for Ambient-Temperature Sodium-Ion Batteries, Chemistry of Materials 28(1) (2016) 106-116. https://doi.org/https://doi.org/https://doi.org/https://doi.org/10.1021/acs.chemmater.5b03276. [46] W. Kang, Z. Zhang, P.-K. Lee, T.-W. Ng, W. Li, Y. Tang, W. Zhang, C.-S. Lee, D.Y. Wai Yu, Copper substituted P2-type Na_{0.67}Cu_xMn_{1-x}O₂: a stable high-power sodium-ion battery cathode, Journal of Materials Chemistry A 3(45) (2015) 22846-22852. https://doi.org/https://doi.org/10.1039/C5TA06371J.

[47] T. Chen, W. Liu, F. Liu, Y. Luo, Y. Zhuo, H. Hu, J. Guo, J. Yan, K. Liu, Benefits of Copper and Magnesium Cosubstitution in Na_{0.5}Mn_{0.6}Ni_{0.4}O₂ as a Superior Cathode for Sodium Ion Batteries, ACS Applied Energy Materials 2(1) (2019) 844-851. https://doi.org/10.1021/acsaem.8b01909.

[48] T. Chen, W. Liu, Y. Zhuo, H. Hu, M. Zhu, R. Cai, X. Chen, J. Yan, K. Liu, Single-phase P2-type layered oxide with Cu-substitution for sodium ion batteries, Journal of Energy Chemistry 43 (2020) 148-154. https://doi.org/https://doi.org/10.1016/j.jechem.2019.08.016. [49] X. Wu, G.-L. Xu, G. Zhong, Z. Gong, M.J. McDonald, S. Zheng, R. Fu, Z. Chen, K. Amine, Y. Yang, Insights into the Effects of Zinc Doping on Structural Phase Transition of P2-Type Sodium Nickel Manganese Oxide Cathodes for High-Energy Sodium Ion Batteries, ACS Applied Materials & Interfaces 8(34) (2016) 22227-22237.

[50] X.-H. Zhang, W.-L. Pang, F. Wan, J.-Z. Guo, H.-Y. Lü, J.-Y. Li, Y.-M. Xing, J.-P. Zhang, X.-L. Wu, P2–Na_{2/3}Ni_{1/3}Mn_{5/9}Al_{1/9}O₂ microparticles as superior cathode material for sodium-ion batteries: enhanced properties and mechanism via graphene connection, ACS applied materials & interfaces 8(32) (2016) 20650-20659.

[51] A.R.C. Bredar, A.L. Chown, A.R. Burton, B.H. Farnum, Electrochemical Impedance Spectroscopy of Metal Oxide Electrodes for Energy Applications, ACS Applied Energy

Materials 3(1) (2020) 66-98. https://doi.org/https://doi.org/10.1021/acsaem.9b01965.

[52] L.A. Middlemiss, A.J.R. Rennie, R. Sayers, A.R. West, Characterisation of batteries by electrochemical impedance spectroscopy, Energy Reports 6 (2020) 232-241.

https://doi.org/https://doi.org/10.1016/j.egyr.2020.03.029.

https://doi.org/https://doi.org/10.1021/acs.chemmater.5b04557.

[53] N. Meddings, M. Heinrich, F. Overney, J.-S. Lee, V. Ruiz, E. Napolitano, S. Seitz, G. Hinds, R. Raccichini, M. Gaberšček, J. Park, Application of electrochemical impedance spectroscopy to commercial Li-ion cells: A review, Journal of Power Sources 480 (2020) 228742. https://doi.org/https://doi.org/10.1016/j.jpowsour.2020.228742.

Figure Captions

Fig. 1. XRD patterns showing the phase evolution of (a) x = 0, (b) x = 0.05, and (c) x = 0.10 samples with calcination temperature

Fig. 2. Rietveld refinement profiles of room temperature XRD data for x = 0 and 0.075 samples calcined at 850 °C and 800 °C, respectively.

Fig. 3. Crystal structure of P2-type NNCMT-0.1 visualized using VESTA software package [41].

Fig. 4. SEM micrographs of (a) x = 0 (b) x = 0.05 (c) x = 0.075 samples. (c1)-c(6) EDS maps of x = 0.075 showing the distribution of its constituent elements.

Fig. 5. XPS spectra of as-prepared Na_{0.67}Ni_{0.20}Cu_{0.15}Mn_(0.65-x)Ti_xO₂ samples (x = 0, 0.025, 0.050, 0.075, 0.100).

Fig. 6. Cyclic voltammogram of (a) x = 0 and (b) x = 0.075 samples at scan rate of 0.1 mv/s.

Fig. 7. Galvanometric charge-discharge curves at discharge rates of (a) 0.1C and (b) 1C. (c) The rate capability of the Na_{0.67}Ni_{0.20}Cu_{0.15}Mn_(0.65-x)Ti_xO₂ samples at different C rates. (d) Cyclic performance of the Na_{0.67}Ni_{0.20}Cu_{0.15}Mn_(0.65-x)Ti_xO₂ samples when cycled at 1C for 300 cycles.

Fig. 8. Ex-situ XRD patterns (a) x = 0.075 cathodes during charge(ch)/discharge(dis) cycle at 0.1C with (a1), (a2) showing the magnified view of patterns in the vicinity of (002) and (004) peaks. The Al peaks (marked by \bullet in the Fig. 8) belongs to the Al current collector.

Figure 1

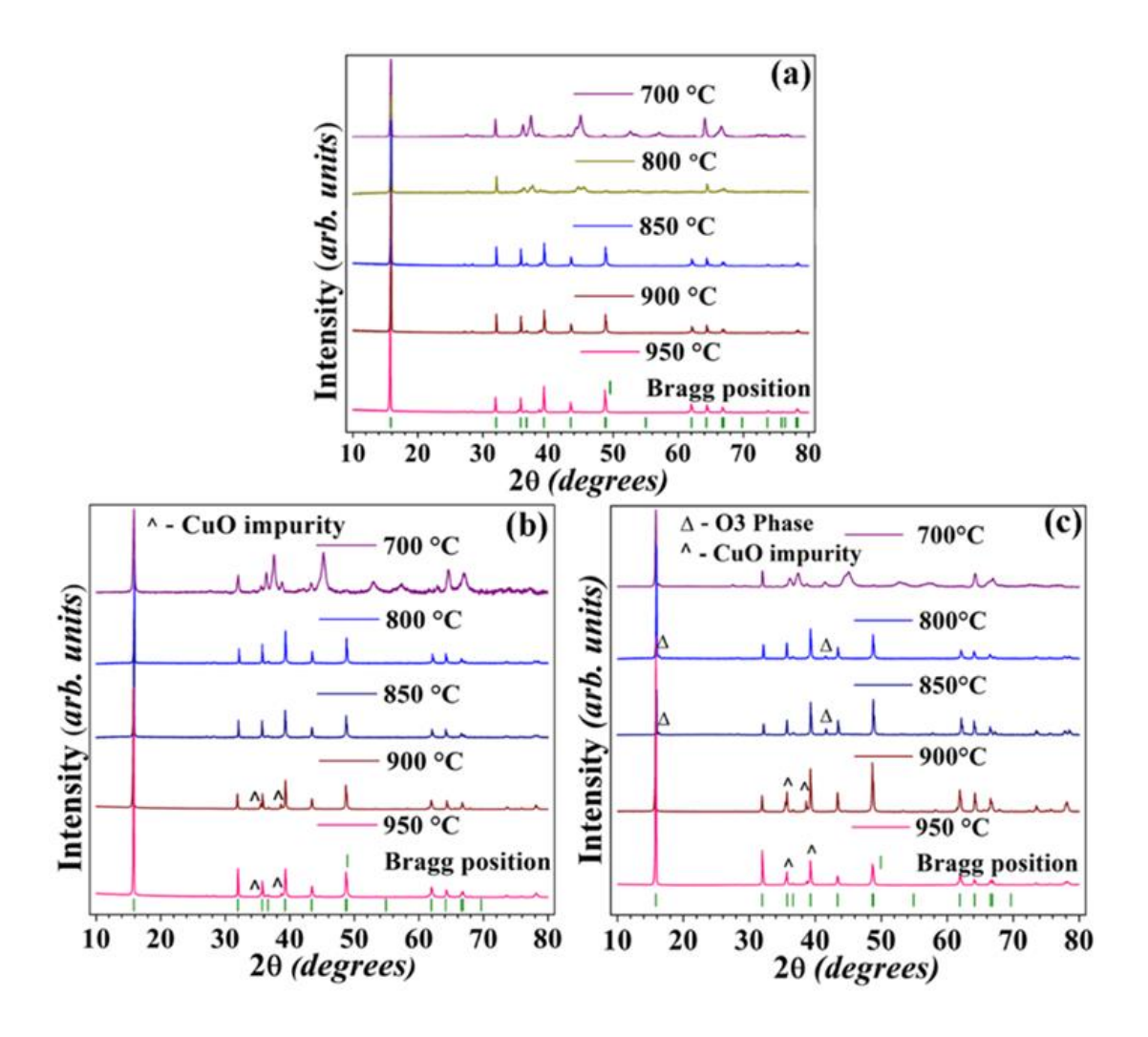


Figure 2

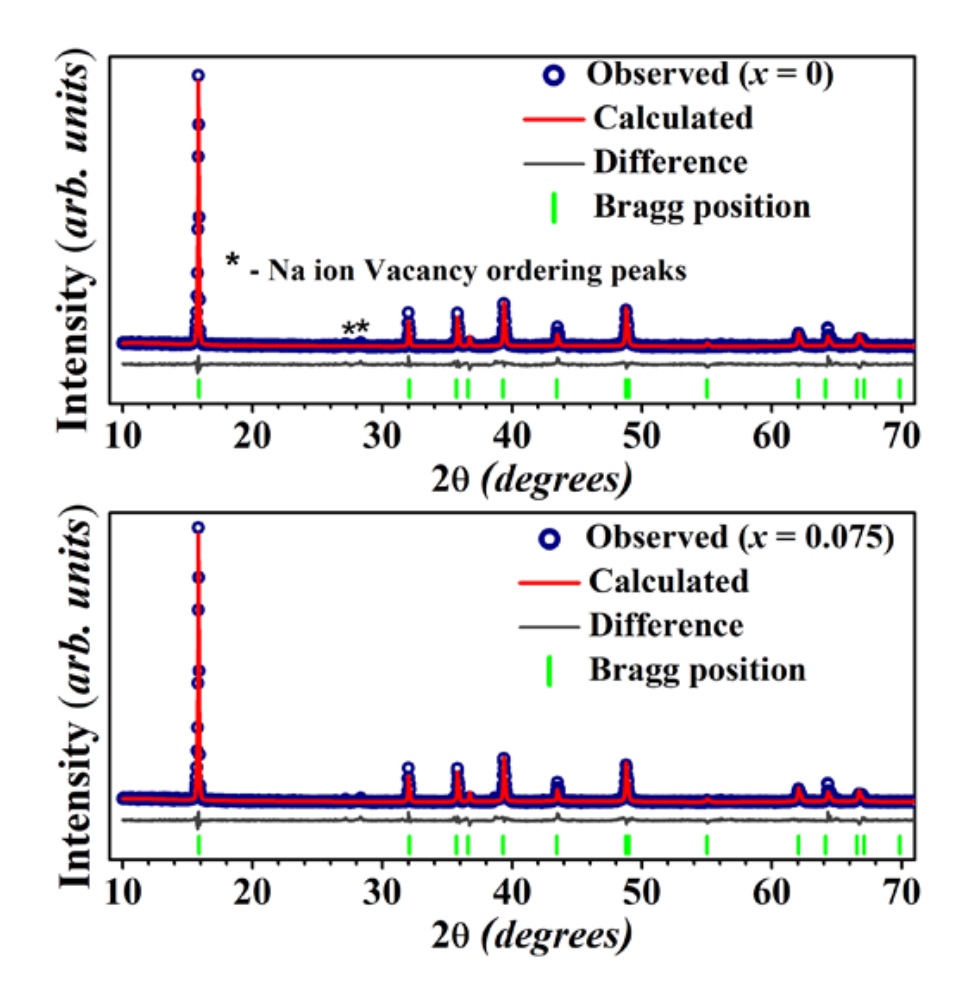


Figure 3

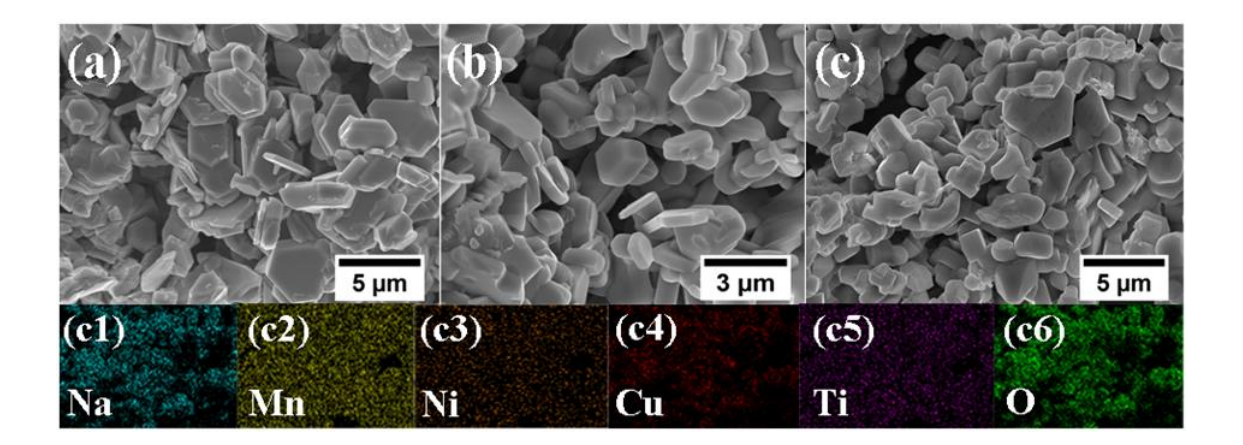


Figure 4

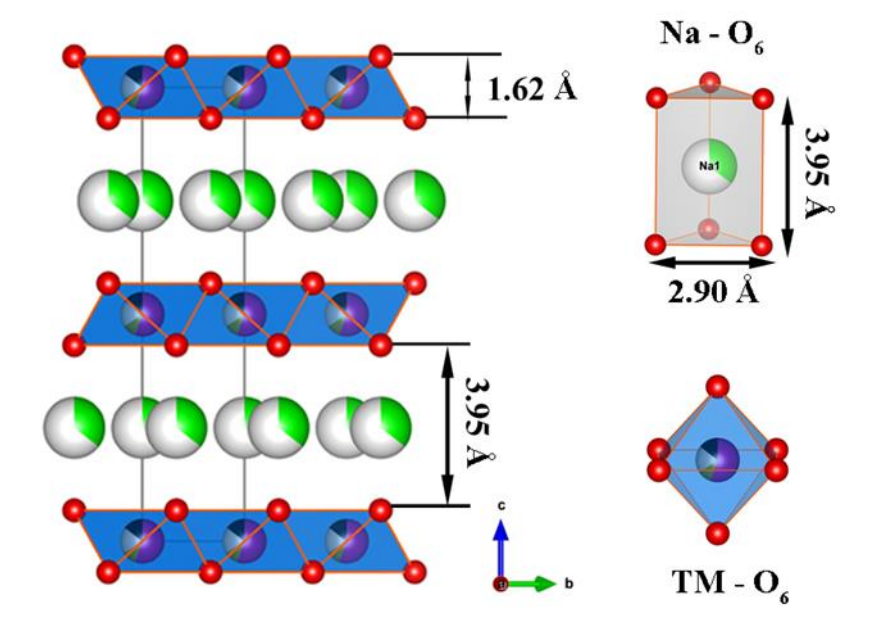


Figure 5

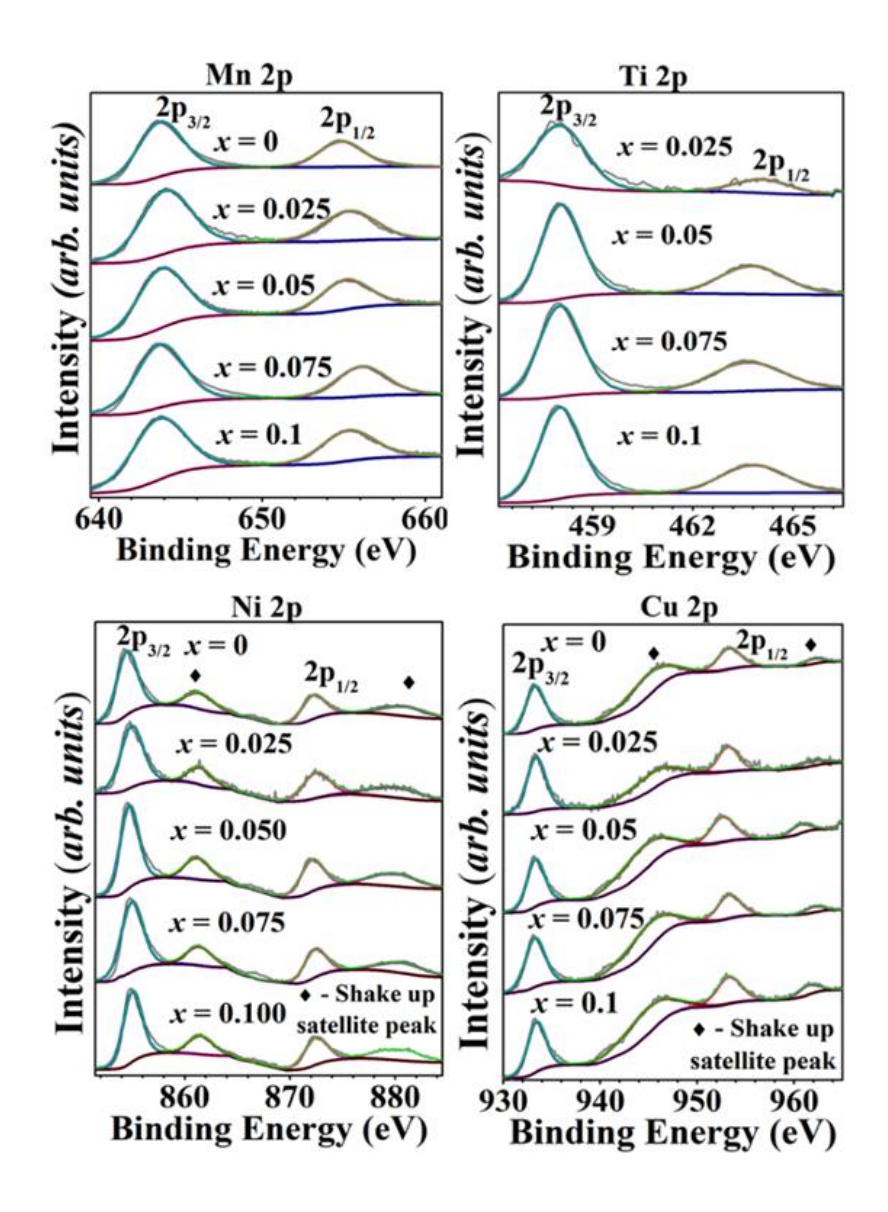


Figure 6

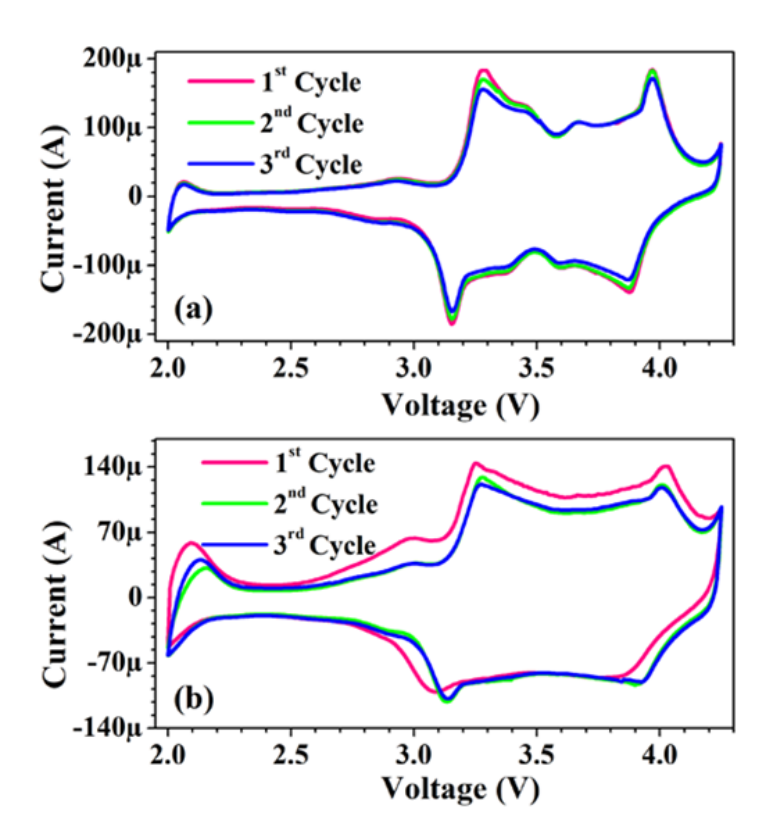


Figure 7

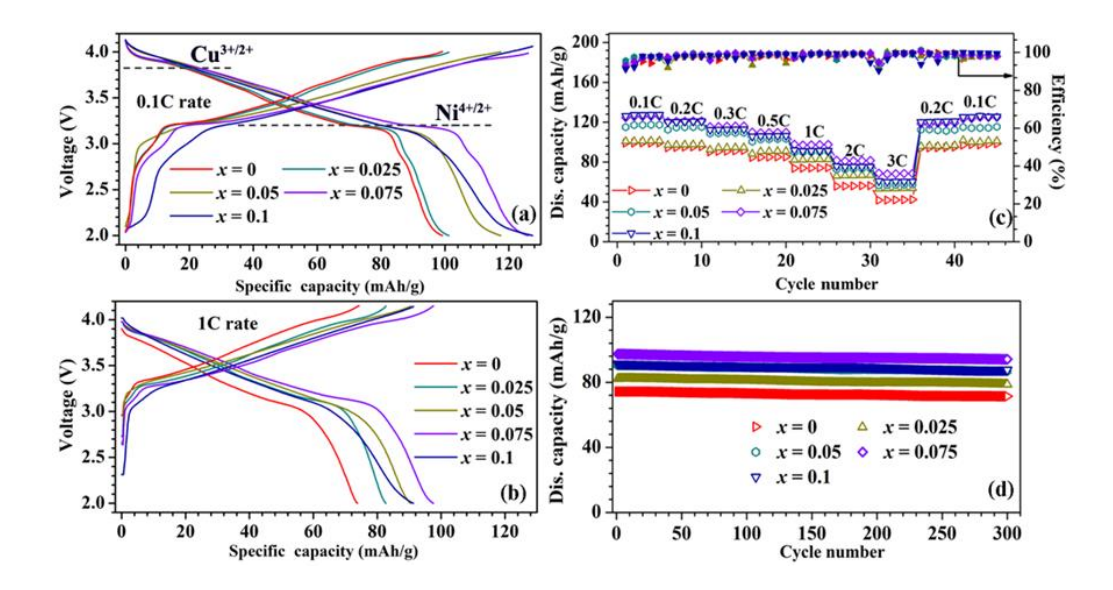
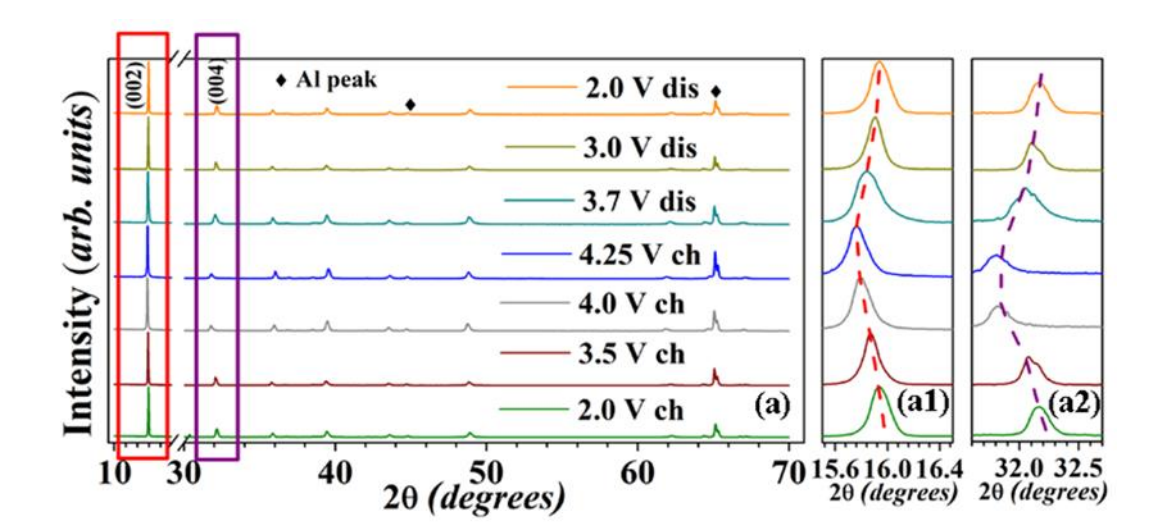


Figure 8



[Supplementary Information]

Enhanced rate performance and specific capacity in Tisubstituted P2-type layered oxide enabled by crystal structure and particle morphology modifications

Hari Narayanan Vasavan^a, Manish Badole^a, Sushmita Dwivedi^a, Deepu Kumar^b, Pradeep Kumar^b, and Sunil Kumar^{a,*}

^a Department of Metallurgy Engineering and Materials Science, Indian Institute of Technology Indore, Simrol, 453552, India.

^b School of Basic Sciences, Indian Institute of Technology Mandi, Mandi, 175005, India

*Corresponding author.

E-mail address: sunil@iiti.ac.in

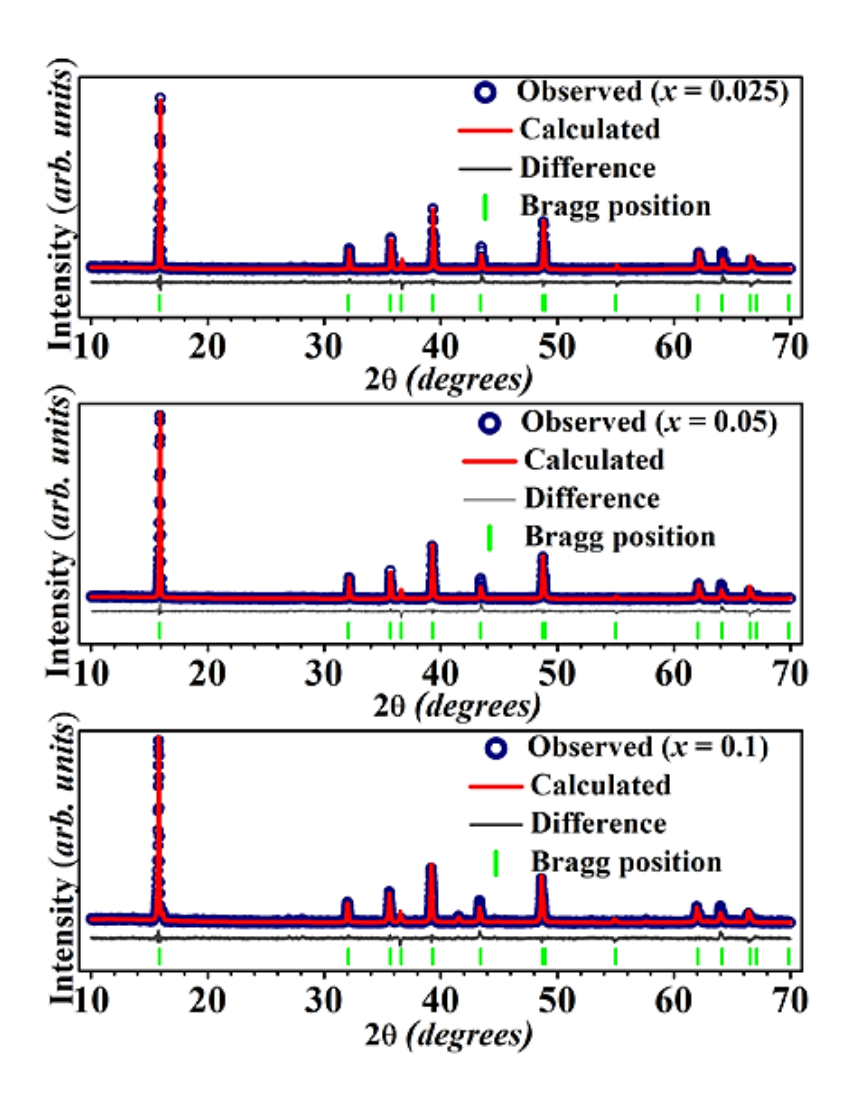


Fig. S1. Rietveld refinement profiles of room temperature XRD data of x = 0.025 calcined at 850 °C, x = 0.050 calcined at 800 °C and x = 0.100 calcined at 800 °C.

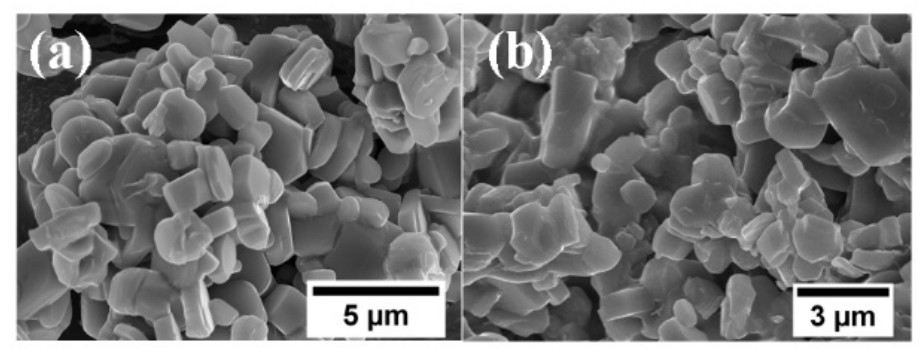


Fig. S2. SEM micrographs of (a) x = 0.025 (b) x = 0.100 samples

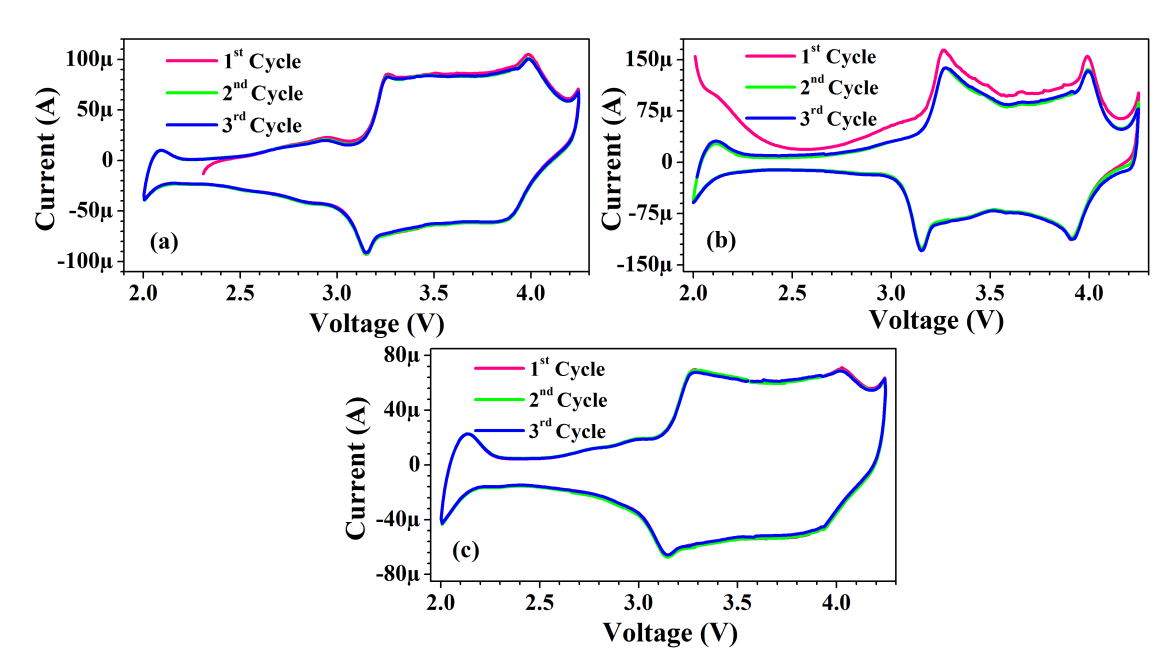


Fig. S3. Cyclic voltammogram of (a) x = 0.025, (b) x = 0.050, and (c) x = 0.100 sample at scan rate of 0.1 mV/s.

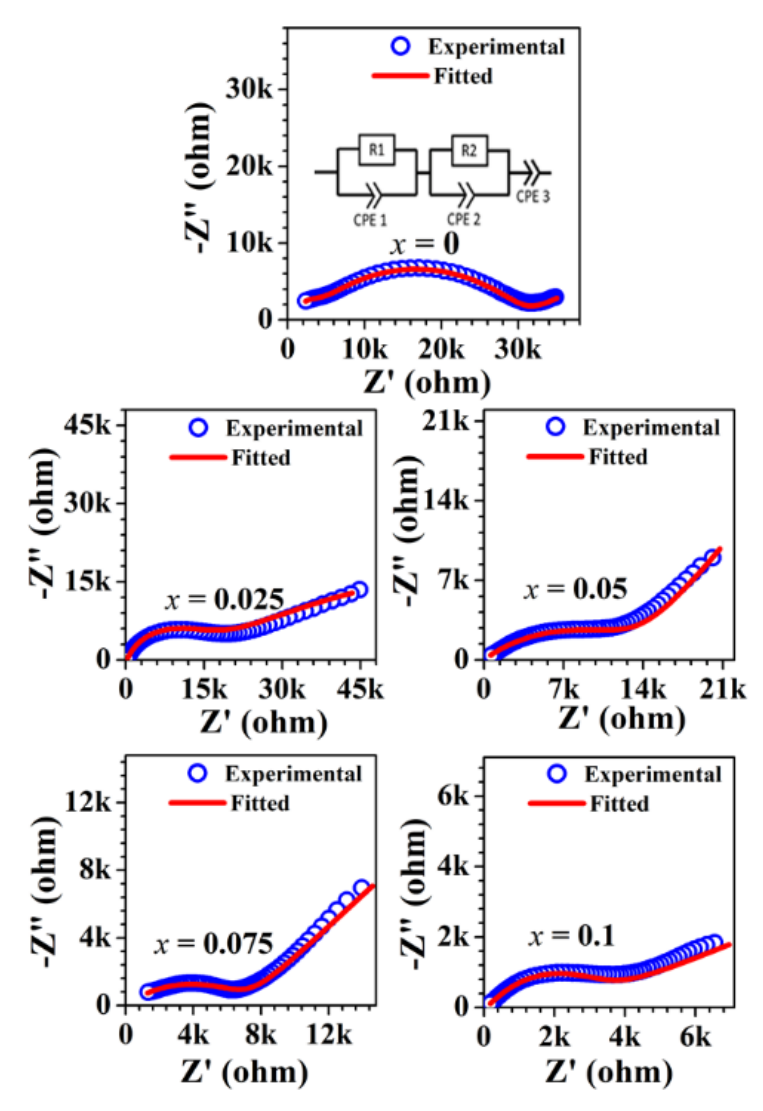


Fig. S4. Nyquist plots of various $Na_{0.67}Ni_{0.20}Cu_{0.15}Mn_{(0.65-x)}Ti_xO_2$ compositions at room temperature. The inset shows the equivalent circuit used to fit the impedance data.

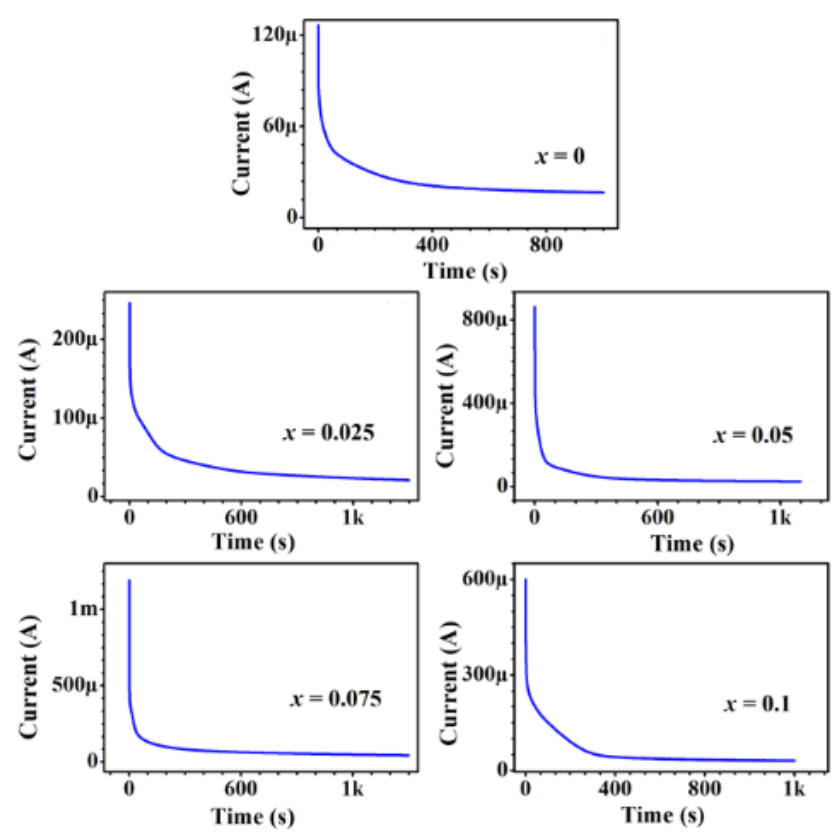


Fig. S5. Chronoamperometry curves of $Na_{0.67}Ni_{0.20}Cu_{0.15}Mn_{(0.65-x)}Ti_xO_2$ sample.

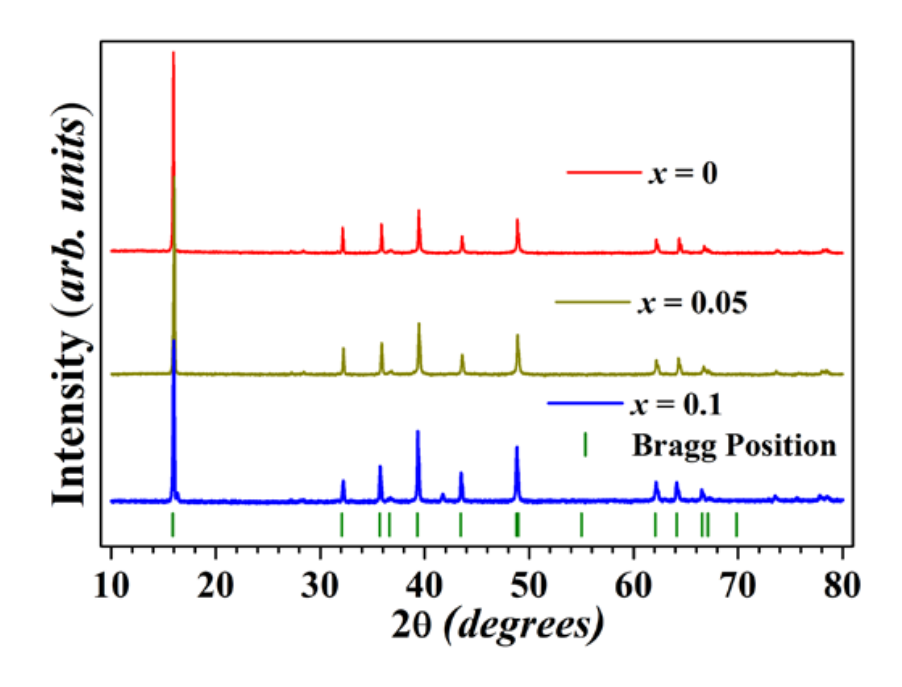


Fig. S6. The XRD patterns of the dried powder samples (x = 0, 0.05, and 0.1) after being stored under DI water for 3 h.

Tables S1-S6. Crystallographic parameters of P2-type NNCMT-*x* obtained from Rietveld refinement of room temperature XRD data.

		S1: x =	0 (space ş	group: <i>P</i> 6 ₃ / <i>mmc</i>)		
Atom	X	y	Z	Occupancy	Site	В
Na1	2/3	1/3	1/4	0.45	2d	1
Na2	0	0	1/4	0.25	2b	1
Mn/ Ti/ Ni/ Cu	0	0	0	0.65/0 /0.20/0.15	2a	1
0	2/3	1/3	0.079	1	4f	1
	;	S2: $x = 0$.025 (spac	e group: <i>P</i> 6 ₃ / <i>mmc</i>)		
Atom	X	y	Z	Occupancy	Site	В
Na1	2/3	1/3	1/4	0.45	2d	1
Na2	0	0	1/4	0.25	2b	1
Mn/ Ti/ Ni/ Cu	0	0	0	0.625/0.025/0.20/0.15	2a	1
0	2/3	1/3	0.078	1	4f	1
	;	S3: x = 0	.050 (spac	e group: P63/mmc)		
Atom	X	y	Z	Occupancy	Site	В
Na1	2/3	1/3	1/4	0.45	2d	1
Na2	0	0	1/4	0.25	2b	1
Mn/ Ti/ Ni/ Cu	0	0	0	0.60/0.05/0.20/0.15	2a	1
0	2/3	1/3	0.078	1	4f	1
	\$	S4: $x = 0$.075 (spac	e group: P63/mmc)		
Atom	X	y	Z	Occupancy	Site	В
Na1	2/3	1/3	1/4	0.45	2d	1
Na2	0	0	1/4	0.25	2b	1
Mn/ Ti/ Ni/ Cu	0	0	0	0.575/0.075/0.20/0.15	2a	1
0	2/3	1/3	0.077	1	4f	1
S5:	x = 0.100	(space g	roup: <i>P</i> 63	/mmc), phase fraction = 9	6.4%	
Atom	X	y	z	Occupancy	Site	В

Na1	2/3	1/3	1/4	0.45	2d	1
Na2	0	0	1/4	0.25	2b	1
Mn/ Ti/ Ni/ Cu	0	0	0	0.55/0.1/0.20/0.15	2a	1
0	2/3	1/3	0.077	1	4f	1
S	66: x = 0.1	100 (spac	e group: R	-3m) phase fraction = 3.	.6%	
Atom	X	y	Z	Occupancy	Site	В
Na1	0	0	1/2	0.70	3b	1
Mn/ Ti/ Ni/ Cu	0	0	0	0.55/0.1/0.20/0.15	3a	1
			0.258	·		